Photon Induced Decoherence of a Transmon Superconducting Charge Qubit

An MPHYS project report

Supervisor: Dr. Peter Leek
Candidate number: 154180
Project number: CMP1502
Word count: 4793

Contents

Abstract

The properties of a transmon qubit inside a 3D superconducting microwave cavity are investigated in the dispersive limit. It is found that the behaviour of the system maps well to a two-state quantum bit (qubit) modelled by the Jaynes-Cummings Hamiltonian. The effective temperature of the qubit is measured as 138.5 ± 20mK, corresponding to an average occupancy of state $|1\rangle$ of $10 \pm 4\%$. An upper limit of $144.5mK$ is placed on the effective cavity temperature for low power (10^{-10}W) experiments, corresponding to a single photon occupancy of less than 3.1%. The effects of decoherence are investigated both at base temperature and when photons are artificially put into the cavity. The T_2 decoherence times of the qubit are found to be on the order of μs when the cavity contained an average of ~ 0.1 photons. The T_2 times are found to decrease with the inverse photon number in a dramatic fashion, consistent with theoretical predictions. It is found that for the device investigated an average number of photons of 0.36 is sufficient to decrease the T_2 time to the sub-microsecond regime and that in low power experiments we have a potential T_2 time $\sim 8\mu s$.

1 Introduction

The search for ever better implementations of two-state quantum systems (or quantum bits) has been a quickly growing area of research in many fields of physics. The ability to accurately control a collection of such quantum systems is essential to building a quantum computer, a device which carries out logical operations on qubit states (we denote the single qubit states $|0\rangle$ and $|1\rangle$). Any system possessing a conserved observable quantity, with at least two sufficiently spaced eigenvalues, is a candidate for implementing a qubit. As a result, realizations of qubits are possible in many areas of physics (for example successful implementations of qubits have used ion traps, NMR and photon polarization states [1]).

A good candidate for an architecture for quantum computing has to fulfil many requirements. In order for operations to be carried out successfully on a set of qubits, they must remain in a well-defined quantum state for the duration. The coupling of such systems to their environment causes them to lose this state information in a process known as quantum decoherence. An important measure of the decoherence of a qubit is the T_2 coherence time. The T_2 time is the characteristic timescale on which the relative phase information for the state $a|0\rangle + b|1\rangle$ is lost (i.e the timescale beyond which the phase difference between the complex numbers a and b is not well known).

As well as having long enough coherence times, it is desirable for a candidate architecture for quantum computation to be scalable in the number of qubits, without sacrificing control fidelity or the ability to prepare them in an ensemble ground state. One promising field for improved qubit designs is the study of superconducting circuits. Because these are solid state systems they lend themselves to scalability in much the same way as modern electronics. These superconducting systems use the charge states of a small superconducting island as the qubit states, in what is known as a *charge qubit*. Charge qubits were first suggested in 1997 [3] and significant work has since been done on improving their T_2 coherence times [2].

In this study we consider a particular type of charge qubit known as a *transmon* [11] coupled to a 3D superconducting microwave cavity. Such systems have been demonstrated to be capable of T_2 times of $\sim 100\mu s$ [4], approaching the regime where the T_2 time is sufficiently long compared to the gate operation time ($10^3 - 10^4$ times the gate operation time, corresponding to $T_2 \sim 20-200\mu s$ for typical systems [4] [13]).

An important source of decoherence is the presence of photons in the cavity, either as a result of thermal excitation or from the measurement signals themselves. As well as this, thermal excitations of the qubit itself contribute significantly to decoherence. We investigate the effects of photons in the cavity on the coherence of the qubit system and put limits on the effective temperature of the system components in an effort to better understand how significant each of these effects is. Low effective temperatures are also of critical importance to the task of preparing the qubit in state $|0\rangle$, which it is essential to be able to do in order to carry out logical operations.

Section 2 covers some of the theory behind the coupling of a qubit to a microwave cavity and explains how this enables measurement of the state of the system, some of the theory behind the transmon qubit design is also explained. In section 3 the experimental setup that enables measurements is explained. Then in section 4 the results and analysis of experiments that characterize the properties of the qubit-cavity system are presented including an investigation into the aforementioned decoherence effects.

2 Theoretical background

In order to model the interaction of a qubit with a microwave cavity, we derive an appropriate Hamiltonian (adapting a derivation given in [5]). The first stage is to derive the Hamiltonian describing quantized electromagnetic excitations of the cavity (without a qubit).

2.1 Cavity field quantization

We begin with the case of a radiation field confined to a one-dimensional cavity with perfectly conducting walls at $z = 0$ and $z = L$.
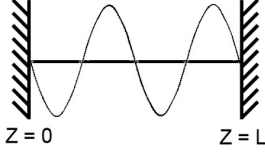

Figure 1: A cavity

We solve the (sourceless) Maxwell's equations within the cavity subject to the boundary condition that the electric field must vanish at the cavity walls:

$$\vec{E}(z = 0, L) = \vec{0} \tag{1}$$

Assuming an electric field polarized along the x axis, we obtain the single-mode solution

$$E_x(z, t) = \left(\frac{2\omega_c^2}{V\epsilon_0}\right)^{\frac{1}{2}} q(t)\sin(kz). \tag{2}$$

Where w_c is the frequency of the mode, $k = w_c/c$ is the corresponding wavenumber and V is the effective volume of the cavity. q(t) is some arbitrary time dependent function with the dimensions of length which will play the role of a canonical position. The magnetic field is then polarized along y:

$$B_y(z, t) = \frac{\mu_0\epsilon_0}{k}\left(\frac{2\omega_c^2}{V\epsilon_0}\right)^{\frac{1}{2}} \dot{q}(t)\cos(kz) \tag{3}$$

Note the appearance of $\dot{q}$, which will play the role of a canonical momentum. The field energy is given by

$$H = \frac{1}{2}\int d^3\vec{r}\left[\epsilon_0 E_x^2(\vec{r}, t) + \frac{1}{\mu_0}B_y^2(\vec{r}, t)\right]. \tag{4}$$

It is straightforward to show that

$$H = \frac{1}{2}(\dot{q}^2 + w_c^2 q^2). \tag{5}$$

We see that this system is formally equivalent to a harmonic oscillator of unit mass. Promoting the canonical quantities to operators ($q \to \hat{q}$, $\dot{q} \to \hat{p}$) and introducing the annihilation and creation operators:

$$\hat{a} = (2\hbar\omega_c)^{-\frac{1}{2}}(\omega_c\hat{q} + i\hat{p}) \tag{6}$$

$$\hat{a}^\dagger = (2\hbar\omega_c)^{-\frac{1}{2}}(\omega_c\hat{q} - i\hat{p}) \tag{7}$$

We obtain an expression for the free cavity Hamiltonian:

$$\hat{H}_c = \hbar\omega_c(\hat{a}^\dagger\hat{a} + \frac{1}{2}). \tag{8}$$

Where the operator $\hat{a}^\dagger\hat{a} \equiv \hat{n}$ is the number operator for photons in the cavity, each having energy $\hbar\omega_c$. The electric and magnetic field operators then become:

$$\hat{E}_x(z, t) = \left(\frac{\hbar\omega_c}{\epsilon_0 V}\right)^{\frac{1}{2}}(\hat{a} + \hat{a}^\dagger)\sin(kz) \tag{9}$$

$$\hat{B}_y(z, t) = \frac{\mu_0}{k}\left(\frac{\epsilon_0\hbar\omega_c^3}{V}\right)^{\frac{1}{2}}i(\hat{a}^\dagger - \hat{a})\sin(kz) \tag{10}$$

2.2 Coherent cavity excitations

A natural way to think about exitations of a cavity is in terms of the photon number states $|n\rangle$ defined by $\hat{n}|n\rangle = n|n\rangle$. The states $|n\rangle$ are clearly energy eigenstates with energies $E_n = \hbar\omega_c(n + \frac{1}{2})$. However from equation 9 we see that

$$\langle n|\hat{E}_x(z, t)|n\rangle = 0. \tag{11}$$

These states do not obey the correspondence principle, as in the classical limit we require $\langle\hat{E}_x\rangle$ to be given by equation 2. This classical limit corresponds to the operators $\hat{a}, \hat{a}^\dagger$ being replaced by some continuous variables α, α^* (i.e. the reverse of what we did in section 2.1). From equations 9 and 10 we see that this replacement is necessary to produce a classical field. One way to make this replacement is to seek states $|\alpha\rangle$ such that $\hat{a}|\alpha\rangle = \alpha|\alpha\rangle$, i.e. eigenstates of the annihilation operator. We call these states 'coherent' states. It can be shown that (see appendix A.1):

$$|\alpha\rangle = e^{-\frac{1}{2}|\alpha|^2}\sum_{n=0}^{\infty}\frac{\alpha^n}{\sqrt{n!}}|n\rangle \tag{12}$$

$$\langle\alpha|\hat{E}_x|\alpha\rangle = 2Re[\alpha]\left(\frac{\hbar\omega_c}{\epsilon_0 V}\right)^{\frac{1}{2}}\sin(kz) \tag{13}$$

$$\langle\alpha|\hat{n}|\alpha\rangle \equiv \bar{n} = |\alpha|^2 \tag{14}$$

Equation 13 shows that the states $|\alpha\rangle$ indeed correspond to classical excitations of the cavity, equation 14 is the expression for the expected number of photons in the cavity for a particular coherent state. It is also interesting to note that the probability of observing n photons in the cavity is given by the Poisson distribution:

$$P_n = |\langle n|\alpha\rangle|^2 = e^{-\bar{n}}\frac{\bar{n}^n}{n!} \tag{15}$$

2.3 Interaction with a qubit

Having derived the Hamiltonian for the cavity alone in section 2.1, we now wish to determine the interaction Hamiltonian, $\hat{H}_I$, coupling the cavity to a qubit inside. Denoting the qubit electric dipole $\hat{\mathbf{d}}$, $\hat{H}_I$ is given by

$$\hat{H}_I = -\hat{\mathbf{d}} \cdot \hat{\mathbf{E}} = \hat{d}s(\hat{a} + \hat{a}^\dagger). \tag{16}$$

where

$$s = -\left(\frac{\hbar\omega_c}{\epsilon_0 V}\right)^{\frac{1}{2}} \sin(kz) \tag{17}$$

and $\hat{d} = \hat{\mathbf{d}} \cdot \hat{\mathbf{x}}$. Introducing the qubit states $|0\rangle$ and $|1\rangle$ and using $\hat{1} = \sum_{n\in\{0,1\}} |n\rangle \langle n|$,

$$\hat{d} = \sum_{n,m\in\{0,1\}} |n\rangle \langle n| \hat{d} |m\rangle \langle m|. \tag{18}$$

We note that by parity $\langle 1| \hat{d} |1\rangle = \langle 0| \hat{d} |0\rangle = 0$, so that the above becomes

$$\hat{d} = |0\rangle \langle 0| \hat{d} |1\rangle \langle 1| + |1\rangle \langle 1| \hat{d} |0\rangle \langle 0|. \tag{19}$$

By considering equation 16 we see that $\hat{d}$ is necessarily Hermitian and so we may write $d \equiv \langle 1| \hat{d} |0\rangle = \langle 0| \hat{d} |1\rangle$ and obtain

$$\hat{d} = d |0\rangle \langle 1| + d |1\rangle \langle 0| = d(\hat{\sigma}_- + \hat{\sigma}_+). \tag{20}$$

Where we have defined the qubit raising and lowering operators $\hat{\sigma}_+ = |1\rangle \langle 0|$ and $\hat{\sigma}_- = |0\rangle \langle 1|$. Defining the coupling strength $g \equiv \frac{1}{\hbar}ds$, the interaction Hamiltonian is then

$$\hat{H}_I = \hbar g(\hat{\sigma}_+ + \hat{\sigma}_-)(\hat{a} + \hat{a}^\dagger). \tag{21}$$

2.4 The Jaynes-Cummings Hamiltonian

The last piece of the puzzle is the free-qubit Hamiltonian. Introducing the operator $\hat{\sigma}_3 = |1\rangle \langle 1| - |0\rangle \langle 0|$ and defining the zero of the qubit to be halfway between the levels $|1\rangle$ and $|0\rangle$, the free qubit Hamiltonian is

$$\hat{H}_q = \frac{1}{2}\hbar\omega_q\hat{\sigma}_3. \tag{22}$$

Where ω_q is the transition frequency $|0\rangle \rightarrow |1\rangle$. Combining the free field (dropping the zero point energy), free qubit and interaction terms we obtain the full Hamiltonian for the system:

$$\hat{H} = \hat{H}_c + \hat{H}_q + \hat{H}_I \tag{23}$$

$$= \hbar\omega_c\hat{a}^\dagger\hat{a} + \frac{1}{2}\hbar\omega_q\hat{\sigma}_3 + \hbar g(\hat{\sigma}_+ + \hat{\sigma}_-)(\hat{a} + \hat{a}^\dagger). \tag{24}$$

We see that the term proportional to $\hat{\sigma}_+\hat{a}^\dagger$ corresponds to exiting both the qubit and the cavity. Similarly the term $\hat{\sigma}_-\hat{a}$ corresponds to de-exiting both. It is clear that

these terms do not conserve energy and so we shall ignore them (this is equivalent to making a rotating wave approximation). This leads to the Jaynes-Cummings (JC) Hamiltonian:

$$\hat{H}_{JC} = \hbar\omega_c\hat{a}^\dagger\hat{a} + \frac{\hbar}{2}\omega_q\hat{\sigma}_3 + \hbar g(\hat{\sigma}_+\hat{a} + \hat{\sigma}_-\hat{a}^\dagger). \tag{25}$$

2.5 Interpreting the JC Hamiltonian

In order to obtain some insight into the properties of the JC Hamiltonian and how it may be probed experimentally, it is useful to make the unitary transformation [10]:

$$\hat{U} = exp\left[\frac{g}{\Delta}(\hat{a}\hat{\sigma}_+ - \hat{a}^\dagger\hat{\sigma}_-)\right]. \tag{26}$$

Where $\Delta \equiv \omega_q - \omega_c$ is the detuning of the qubit from the cavity. We take $\frac{g}{\Delta} \ll 1$ (large detuning) and obtain to second order in $\frac{g}{\Delta}$:

$$\hat{U}\hat{H}_{JC}\hat{U}^\dagger \approx \hbar\omega_c\hat{a}^\dagger\hat{a} + \frac{\hbar}{2}\omega_q\hat{\sigma}_3 + \frac{\hbar g^2}{\Delta}\left(\hat{a}^\dagger\hat{a} + \frac{1}{2}\right)\hat{\sigma}_3 \equiv \hat{H}'_{JC} \tag{27}$$

This is known as the dispersive limit. It is easiest to interpret the interaction term $\frac{\hbar g^2}{\Delta}(\hat{a}^\dagger\hat{a} + \frac{1}{2})\hat{\sigma}_3$ in this expression by grouping it with the other terms in different ways, leading to the two following forms:

$$\hat{H}'_{JC} = \hbar\left(\omega_c + \frac{g^2}{\Delta}\hat{\sigma}_3\right)\hat{a}^\dagger\hat{a} + \frac{\hbar}{2}\omega'_q\hat{\sigma}_3 \tag{28}$$

$$\hat{H}'_{JC} = \hbar\omega_c\hat{a}^\dagger\hat{a} + \frac{\hbar}{2}\left(\omega'_q + \frac{2g^2}{\Delta}\hat{a}^\dagger\hat{a}\right)\hat{\sigma}_3 \tag{29}$$

where $\omega'_q \equiv \omega_q + \frac{g^2}{\Delta}$ is the lamb-shifted qubit frequency.

Equation 28 shows how the interaction term can be interpreted as the qubit shifting the cavity frequency by $\delta \equiv \frac{2g^2}{\Delta}$ as it transitions between $|0\rangle$ ($\hat{\sigma}_3 = -1$) and $|1\rangle$ ($\hat{\sigma}_3 = 1$). Equation 29 shows how the same term can also be interpreted as each photon in the cavity shifting the qubit frequency by δ. We see that these properties allow us to construct an experimental setup that can both probe the qubit state by measuring the cavity frequency, as well as probe the photon occupancy of the cavity by measuring the qubit frequency.

2.6 The effect of cavity photons on T_2 times

A major aim of this project is to demonstrate the relationship between the average photon number in the cavity and the T_2 time of the qubit. This will enable us to get a feel for how dramatically these photons cause the decoherence of the system. The theoretical decay of the qubit phase decoherence is proportional to [12]:

$$exp\left[-\frac{(\bar{n}_+ + \bar{n}_-)\kappa\delta^2 t}{\kappa^2 + \delta^2 + 4\Delta_r^2}\right] \tag{30}$$

3

Where $\bar{n}_{\pm}$ is the average number of photons in the cavity when the qubit is exited($+$) or in the ground state($-$), κ is the rate of loss of photons from the cavity and Δ_r is the detuning of the drive that is exiting the cavity photons from the cavity frequency ω_c. In our investigation $\Delta_r = 0$ and $\bar{n}_- \approx \bar{n}_+$. We expect the phase coherence to scale as $\exp(-t/T_2)$, combining this with equation 30 we obtain a theoretical relationship between $\bar{n}$ and T_2:

$$T_2 \propto \frac{1}{\bar{n}} \qquad (31)$$

2.7 The transmon qubit

The qubit design that we will be using is called a *transmon* [11]. The design of the transmon is closely derived from a Cooper pair box (fig. 2.a), a superconducting island formed between the plate of a capacitor (the gate capacitor C_g) and one side of a Josephson junction (a thin insulating barrier between two pieces of superconductor). The transmon is a modified version of this design (fig. 2.b), modified in order to reduce the effect of fluctuations in the gate capacitor charge $n_g = V_g C_g / 2e$.
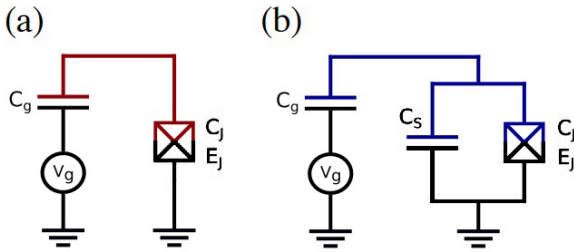

Figure 2:
a) Cooper pair box effective circuit
b) Transmon effective circuit
Both with superconducting island highlighted
(figure reproduced from [7] with modifications)

The mechanics of this system is analysed in detail in appendix A.2, leading to the energy levels shown in 3. Adding the capacitance C_s in parallel with the Josephson junction has the effect of increasing the ratio of the Josephson energy E_j to the energy of a single cooper pair on the island (the *charging energy E_c*). This leads to the modification of the energy levels shown in progression in figure 3.
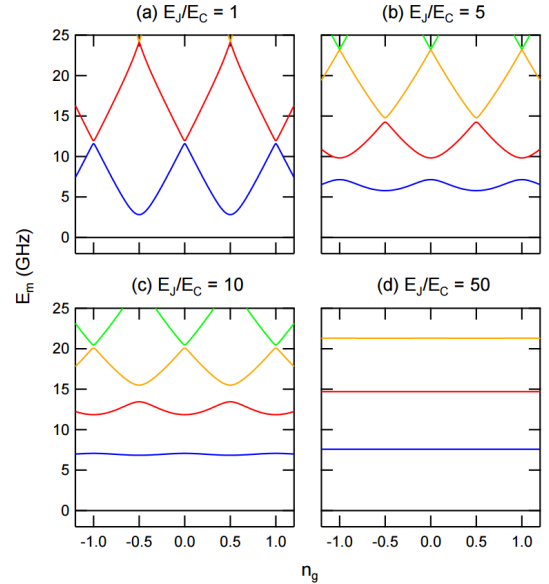

Figure 3: The energy levels of a charge qubit, from the Cooper pair box regime ($E_J/E_C \sim 1$) to the transmon regime ($E_J/E_C \sim 50$). Figure reproduced from [7].

In order to use the simple Cooper pair box as a qubit, it is necessary to set a working point or "sweet spot", by setting V_g to choose a particular value of n_g. We see that noise in the value of n_g (charge noise) will cause us to stray from this working point and modify the energy levels of the system; this contributes significantly to decoherence. By increasing the ratio of E_J/E_C (moving into the transmon regime) we eliminate this problem, as the energy levels are approximately independent of n_g in this limit.

We also see that the levels of this system contain an anharmonicity, meaning that the $|0\rangle \rightarrow |1\rangle$ transition is well isolated from the $|1\rangle \rightarrow |2\rangle$, and higher, transitions. This means that the system is well approximated by the simple two-level description used so far.

3 Experimental setup

3.1 Refrigeration

To perform cavity QED experiments, the qubit-cavity system would ideally be prepared with the qubit in state $|0\rangle$ and with no photons in the cavity. In order to get as close to this as possible the system must be cooled such that $k_b T \ll \hbar\omega_q, \hbar\omega_c$. In our case $\omega_q < \omega_c$ with $\omega_q/2\pi \approx$ 6.525GHz so the critical temperature $T_c = \hbar\omega_q/k_b \approx$ 313mK. In order to achive this a Helium dilution refrigerator is used, with several cooling stages (see figure 4.a).
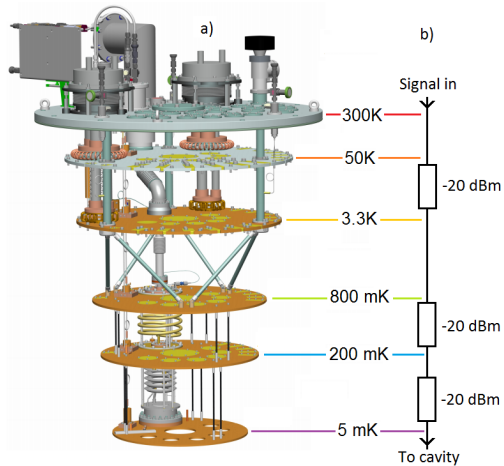
Figure 4: a) The Helium dilution refrigerator, without radiation shielding. b) The input line attenuation. (figure reproduced from [8] with modifications)

The main sources of thermal noise at the coldest stage are radiation and thermal noise being transmitted along the measurement cables used to send signals to the system. In order to reduce the radiation noise the entire fridge assembly is surrounded by a radiation shield (which doubles as a vacuum chamber). As well as this the individual cavity-qubit systems are surrounded by their own radiation shields made from a special alloy Amumetal that is annealed in a dry Hydrogen atmosphere for optimum magnetic permeability at cryogenic temperatures. The thermal noise from the cables is reduced by attenuating the input cables at each cryogenic stage, so that the black-body radiation from components at one stage is attenuated before it reaches the next stage (see figure 4.b).

3.2   Readout

In order to measure the absorption spectrum of the cavity-qubit system (and thus measure the qubit-cavity states using the results of section 2.5), we need to be able to send in microwave signals at a range of frequencies. As well as this, we need to be able to send qubit control pulses into the cavity (in the form of π pulses etc.) to carry out more complicated experiments (such as the Ramsey experiments carried out in section 4.7). To complicate matters, because we operate the cavity in the few-photon regime, these signals need to be extremely small by the time they reach the cavity (on the order 10^{-17}W). As a result, we need to be able to send very precisely controlled microwave signals to the cavity-qubit system. Controlling and measuring such small signals in the GHz regime is a reasonably complex signal processing task, which we achieve using a combination of techniques including IQ-Mixing, high quality amplification and Heterodyne detection. These are explained in more detail in appendix A.3.

As a result of the transmitted signal being extremely small as it leaves the cavity, it is dominated by noise picked up on its way out of the fridge. This means that we must average the results of several tens of thousands of experiments to achieve acceptable signal to noise ratios (most of the measurements carried out in this study were averaged hundreds of thousands of times). As a result a single run could take days. In order to reduce this somewhat we take advantage of a method that we call 'high power readout'. This method relies on the fact that the absorption of the cavity at high powers (far beyond the regime where the models derived in section 2 work) exhibits a bifurcation as a result of the qubit state. The result is that we can run a high power absorption spectrum and see a different result if the qubit is in $|1\rangle$ rather than $|0\rangle$ (see figure 5). This acts as a method of measuring the qubit state.

The physical mechanism behind this bifurcation is not well-understood, but because it happens at higher powers it gives a much better signal to noise ratio. Obviously, the power required is far too high to be present whilst the experiment is underway, so we must use a pulsed measurement scheme. This scheme consists of carrying out the experiment at low power and then sending in a readout pulse at high power immediately afterwards, to collect the results.

3.3   Device parameters

In our case the qubit is designed with a $|0\rangle \rightarrow |1\rangle$ transition frequency of $\omega_q/2\pi \approx 6.525$GHz. The qubit is installed inside an aluminium cavity engineered with a single resonant mode with $\omega_c/2\pi \approx 10.43$GHz.

4   Measurements

4.1   A note on errors

Because of the averaging procedure mentioned in section 3.2 the error bars on a particular data point in all of the plots are exceedingly small (and hence not shown). However, there remains a non-zero amount of noise between the individual data points (as can be seen on the plots). This noise could not be removed by increasing the number of averages taken. In fact, one of the experiments actually showed an increased noise level with more averaging. This leads to the conclusion that the noise is due to effects that fluctuate on a similar timescale to the measurements (several hours), things like fluctuation in the temperature of the lab. This noise level is treated as the error for the purpose of fitting. Derived quantities are quoted with their standard fitting errors.
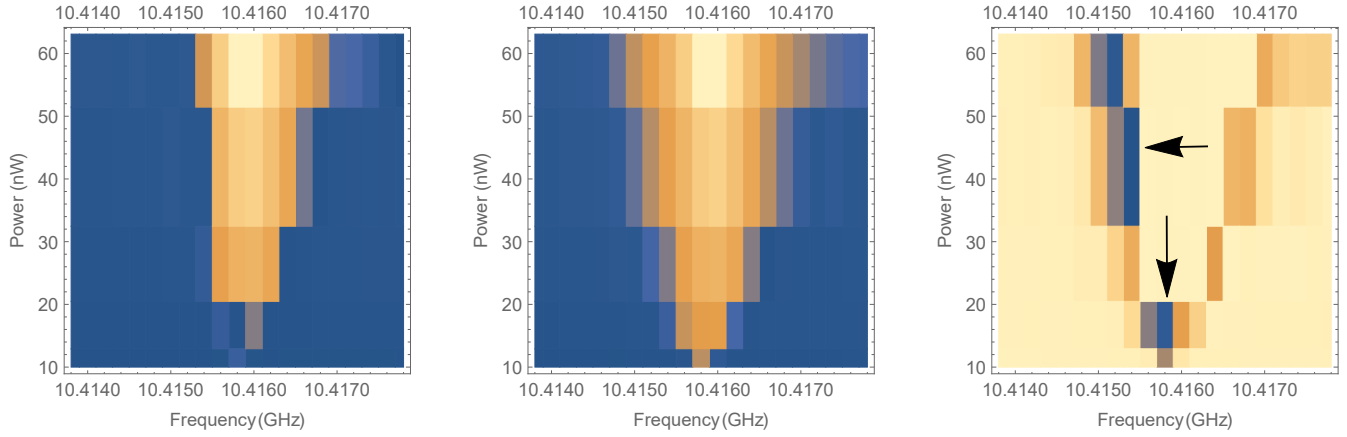
Figure 5: The high-power absorption spectrum of the cavity. From left to right; with the qubit in state $|0\rangle$, with the qubit in state $|1\rangle$, the difference in absorption (with arrows indicating example working points for measurements). The color on the left two figures indicates the absorption strength, white being strong absorption and blue being weak absorption. On the rightmost figure, blue indicates the largest difference

4.2 Measuring ω_q, ω_c

In order to carry out experiments investigating the dynamics of our system it is necessary to know ω_q and ω_c accurately. To find these values we carry out a microwave absorption experiment, expecting to see resonant peaks at the qubit and cavity frequencies. We expect these resonances to be lifetime broadened to a Lorentzian (see appendix A.4).

The absorption spectrum of the qubit is measured in the vicinity of the $|0\rangle \rightarrow |1\rangle$ transition frequency and the results are shown in figure 6. The Lorentzian fit gives $\omega_q/2\pi = 6.524865$ GHz $\pm$ 2.3 kHz. Similarly, the absorption spectrum of the cavity is measured in the vicinity of its resonance and the results are shown in figure 7. The Lorentzian fit gives $\omega_c/2\pi = 10.42862$ GHz $\pm$ 15.7 kHz. This means that our detuning $\Delta = \omega_q - \omega_c$ is given by $\Delta/2\pi$ = -3.90374 GHz $\pm$ 15.9 kHz (Note the minus sign as $\omega_c > \omega_q$).
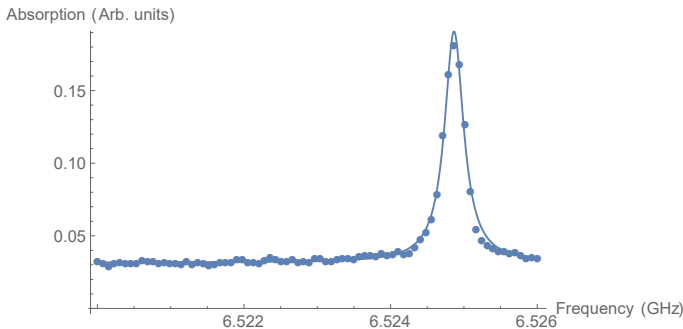

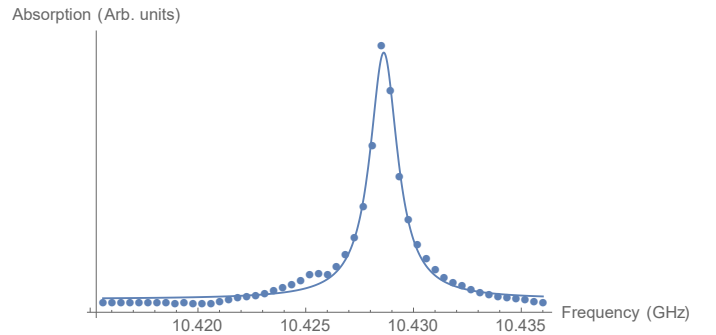Figure 6: Qubit absorption sepctrum with Lorentzian fit.

Figure 7: Resonator absorption sepctrum with Lorentzian fit.

4.3 Measuring the cavity shift $\frac{2g^2}{\Delta}$

Now that we know the qubit and cavity frequencies it is possible to carry out more interesting experiments. Driving the qubit by sending in a signal at ω_q, we can cause transitions $|0\rangle \rightarrow |1\rangle$ so that the qubit has a non-zero probability to be in state $|1\rangle$. According to equation 28 an absorption measurement on the cavity should then show two absorptions, one at the unshifted frequency ω_c corresponding to the qubit in state $|0\rangle$ and one at $\omega_c + 2g^2/\Delta$ corresponding to the qubit in state $|1\rangle$. Note that in our case $\Delta < 0$ so we expect the cavity frequency to be decreased when the qubit is in state $|1\rangle$. The results of such an experiment are shown in figure 8, fit to a pair of Lorentzians. We see that the resonator has indeed been split by the qubit. The fits give a splitting $2g^2/2\pi\Delta$ = -3.21 MHz $\pm$ 32 kHz. Combined with the known detuning Δ we obtain a value for the coupling strength $|g|/2\pi$ = 497.345 MHz $\pm$ 8.9 kHz. This allows us to confirm that we are indeed in the dispersive regime, as $|g|/\Delta \approx 0.02 \ll 1$ as we assumed in section 2.5.
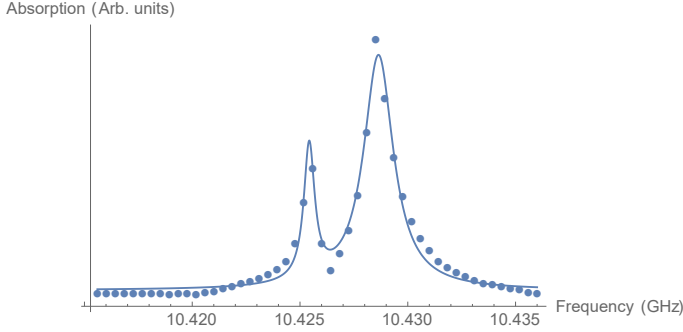
Figure 8: Resonator absorption spectrum, qubit driven, with double Lorentzian fit.

4.4 Measuring the qubit shift

Similarly to the cavity shift experiment carried out in section 4.3 we may measure the shift in qubit frequency due to photons in the cavity predicted by equation 29. In order to do this we drive the cavity at its resonant frequency ω_c, at different drive powers. As the power increases we should see more photons in the cavity, and thus see sequential peaks all separated by $2g^2/2\pi\Delta$. The results of this experiment are shown in figure 9.
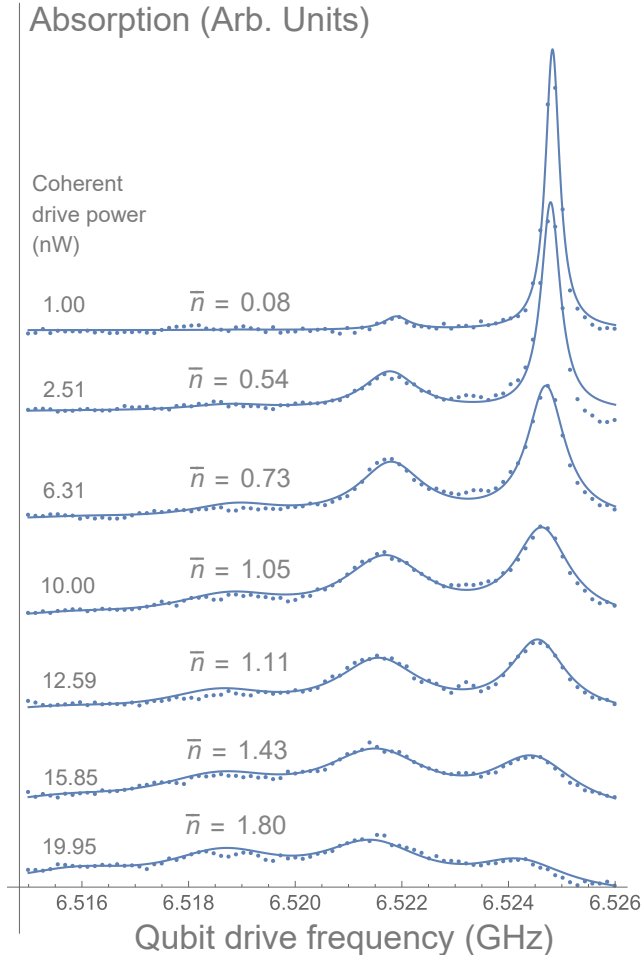

Figure 9: Qubit absorption for different coherently driven powers, with fits to equation 32.

We clearly observe the splitting of the qubit frequency into multiple peaks due to photons in the cavity. The amplitude of each absorption peak will be proportional to the probability that the cavity contains the corresponding number of photons. As we are driving the cavity coherently, we expect to see a Poisson distribution of photon number states as predicted by equation 15. To investigate this the data in figure 9 are fit to the function:

$$A(f) = A_0 \sum_{n=0}^{n_{max}} e^{-\bar{n}} \frac{\bar{n}^n}{n!} \frac{\Gamma_n/2\pi}{\frac{1}{4}\Gamma_n^2 + (f_0 - n\delta - f)^2} \quad (32)$$

Where the widths Γ_n are given (see [12]) by

$$\Gamma_n = \gamma_0 + \Gamma_\Delta(n + \bar{n}) \quad (33)$$

With the fitting parameters

$$A_0, f_0, \delta, \bar{n}, \gamma_0, \Gamma_\Delta. \quad (34)$$

This function is a series of (normalized) Lorentzians centred at the shifted qubit frequencies $f_n = f_0 - n\delta$ with widths given by Γ_n, each occupied according to the Poisson distribution predicted by equation 15. The shift δ should be given by the value predicted by the JC Hamiltonian (i.e $\delta = |2g^2/2\pi\Delta|$) and the unshifted frequency f_0 should correspond to the value found in section 4.2. The results of these fits are shown in figure 9, along with the derived value of $\bar{n}$. The standard fitting errors on $\bar{n}$ are around 3%.

The fits in figure 9 give us a relationship between cavity drive power P and the best fit $\bar{n}$. This relationship is plotted in figure 10. From equations 13 and 14 we see that $\bar{n} \sim |\alpha|^2 \sim |E_x|^2 \sim P$. This explains the linear relationship.
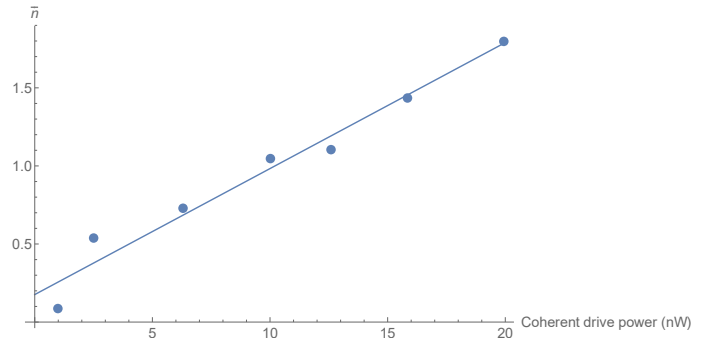

Figure 10: The fitted values for $\bar{n}$ vs drive power, with linear fit

From figure 10 that there is an extrapolated residual number of photons in the cavity when we are not artificially driving the cavity, given by the y intercept of the fit. This is given by $\bar{n}_R = 0.18 \pm 0.08$. These residual photons might be due to a combination of thermal noise being

transmitted down the cables, both from environmental sources and from residual heating due to the drive signal. We do not investigate the source of these residual photons here, but this would be a good topic for further investigation.

Another interesting aspect of the fits in figure 9 is the relationship between the fitted value for the *unshifted* qubit frequency f_0 and the cavity drive power (i.e. the relationship between the frequency of the qubit spectral line corresponding to $n = 0$ and the cavity drive power). This is shown in figure 11. The fitted value of f_0 exhibits a decrease with increased power. This behaviour is due to the classical stark shift of the qubit frequency and is inconsequential to our investigation.
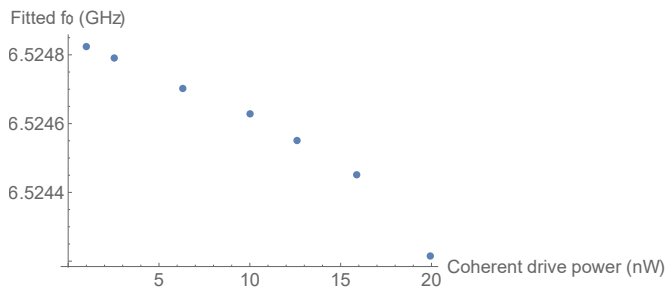

Figure 11: The fitted values for f_0 vs drive power

4.5 Limits on the effective cavity temperature

The effective cavity temperature T_c can contribute to decoherence in the form of thermal cavity excitations, it is also an important measure of how well the system has been cooled. This temperature may be extracted using qubit spectroscopy, with the same experiment as in section 4.2. At higher temperatures we expect to see cavity photons appearing, causing a shift in the qubit frequency. From figure 6 we see that this effect is unresolvable, if it were resolvable we would be able to distinguish a secondary peak at lower frequencies (similar to figure 8). This is because the second peak is attenuated by the boltzmann factor $e^{-\hbar\omega_c/k_b T_c}$.

The fact that a second peak isn't resolvable allows us to place a limit on the effective temperature by considering the noise level in figure 6. The maximum temperature that would be unresolvable is the temperature when the attenuation is equal to the ratio, r, of the noise level to the height of the first peak. This then gives an upper bound on the effective cavity temperature $T_c < \frac{-\hbar\omega_c}{k_b ln(r)}$. As a further correction, the fact that the width of the $n = 1$ peak is greater than the $n = 0$ peak (and therefore the $n = 1$ peak will appear shorter for a given amplitude)

is taken into account using equation 33 and the results of the fit of figure 9. This correction effectively takes account of the fact that we want r to be the photon number probility ratio $r = p_1/p_0$, not simply a ratio of peak heights. This gives $r = \Gamma_1 N/\Gamma_0 H$, where N is the noise level and H is the height of the unshifted peak. From the fits in figure 9 the ratio $\Gamma_1/\Gamma_0 \approx 1.71$. If we use the RMS of the residuals of the fit from figure 6 as our noise level, we obtain $T_c < 144.5$mK. This corresponds to a single photon occupation of less than 3.1%.

4.6 Measuring the effective qubit temperature

The effective temperature of the qubit, T_q, contributes to decoherence in much the same way as the effective cavity temperature. Because it also responsible for thermal excitations $|0\rangle \to |1\rangle$ a low T_c is important for proper initialization of the qubit in state $|0\rangle$. Similarly to the analysis performed in section 4.5 we look at the thermal exitation of the qubit causing a shift in cavity frequency. From figure 7 it is clear that we indeed do see a (small) secondary peak caused by the thermal exitation of the qubit. Fitting this with two Lorentzians produces figure 12.

We can see immediately that this is a better fit than in the preliminary investigation in section 4.2. The resulting ratio of peak amplitudes then gives the effective temperature $T_q = \frac{\hbar\omega_q}{-k_b ln(r)}$ where r is the amplitude ratio of the shifted and unshifted peaks. The fit gives $r = 0.10 \pm 0.04$ which results in $T_q = 138.5 \pm 20 mK$. This corresponds to a probability to be in $|1\rangle$ of $10 \pm 4\%$.
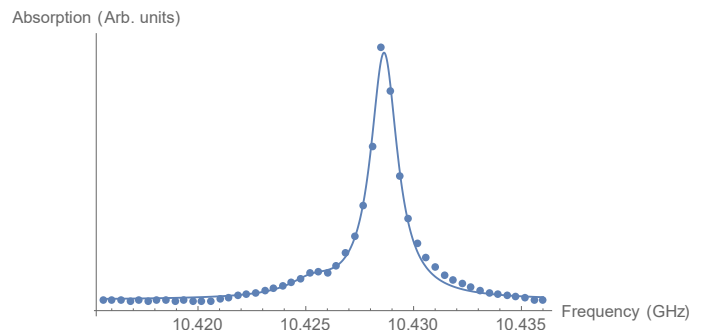

Figure 12: The cavity response with double Lorentzian fit

We expect $T_c = T_q$ as the qubit is inside of the cavity and system has had ample time to thermalize. It is therefore reassuring to note that the value for T_q obtained here is compatible with this expectation given the results of section 4.5 ($T_c < 144.5$mK).

4.7 Measuring the T_2 time of the qubit

An important property of the qubit is the decoherence time T_2. This is the timescale beyond which superposition states of the qubit (such as $\frac{|0\rangle+|1\rangle}{\sqrt{2}}$) are no longer stable. In order to measure the T_2 time of the qubit we use a Ramsey interferometric experiment. The experiment consists of applying a $\pi/2$ pulse to the qubit in state $|0\rangle$ followed by a variable wait time Δt, followed by a further $\pi/2$ pulse and subsequent readout of the qubit state. This experiment is best described by manipulations of the bloch sphere (see figure 13). The qubit can be initialized to $|0\rangle$ by waiting for $t \gg T_1$ where T_1 is the characteristic decay time from $|1\rangle \rightarrow |0\rangle$.
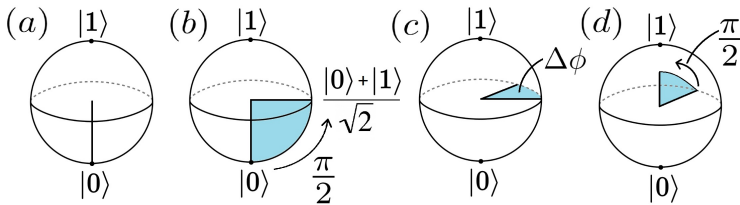
Figure 13: The Ramsey experiment
a) Qubit initialized to $|0\rangle$
b) Apply $\pi/2$ pulse
c) Wait for some time Δt
d) Apply $\pi/2$ pulse

The wait time Δt will induce a phase difference between the states of $\Delta\phi = \omega_q t$. This phase difference will then mean that the subsequent $\pi/2$ pulse will not take the qubit all the way to $|1\rangle$. Consequently, as the phase difference precesses around the Bloch sphere (as we increase Δt), we will see oscillations of the qubit inversion. As the time Δt increases the effects of decoherence will cause the phase difference to tend towards randomness, destroying the coherent oscillations. As a result the inversion oscillations will be enveloped by a factor e^{-t/T_2}. Obviously the oscillations at ω_q are too fast to directly observe on the same timescale as T_2. In order to see oscillations we also drive the qubit at a detuned frequency $\omega_q + \Delta\omega$, as a result we actually see oscillations at the detuning frequency $\Delta\omega$. We choose $\Delta\omega = 10\text{MHz}$.

We carry out such an experiment whilst driving the cavity at various coherent drive powers (as we did in section 4.4). The results of this experiment are shown in figure 14, with fits to an exponential envelope $\sim \exp(-t/T_2)$. The data was truncated before extreme decoherence for the purpose of fitting (for example just before $2\mu s$ for a drive power of 6.31 nW).
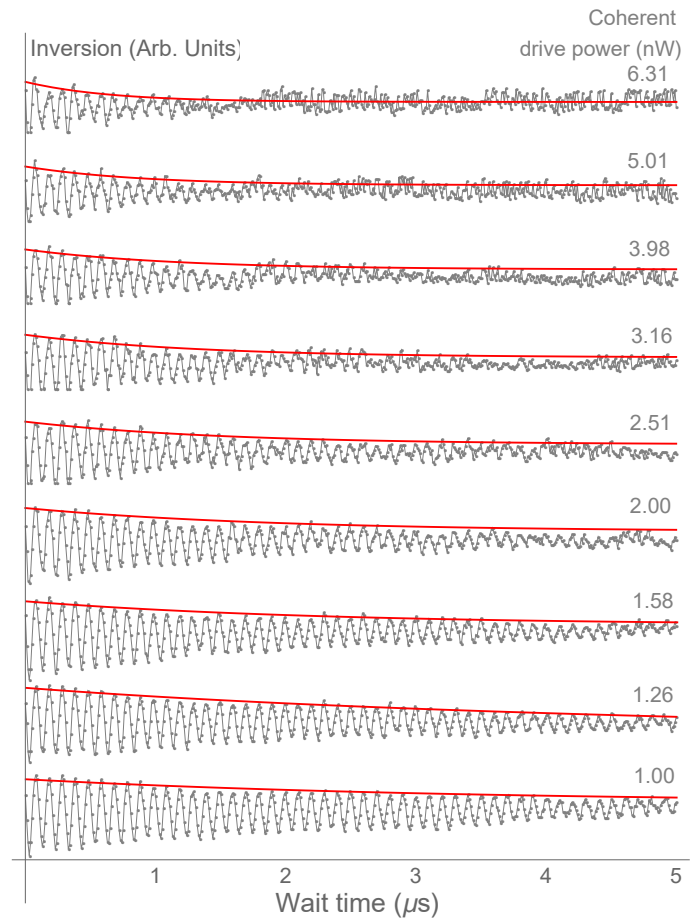
Figure 14: Ramsey oscialltions for different coherent drive powers, with T_2 envelope fit.

It is clear to see the decoherence of the qubit occurring at earlier times for higher coherent drive powers. This is to be expected due to the increased source of decoherence from the increased average photon number. Fitting an exponential of the form e^{-t/T_2} to the envelope of the Ramsey oscillation gives the T_2 times shown in figure 15. As a result of the coherent power being proportional to the average photon count (see figure 10) we expect the T_2 times to scale as $1/\text{power}$ from equation 31.
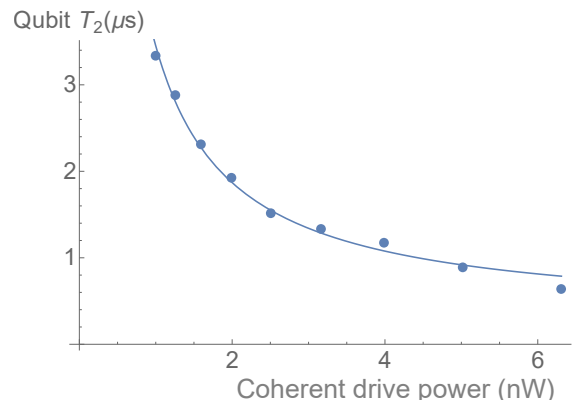
Figure 15: The T_2 coherence times of the qubit for different coherent cavity driving powers (with $1/\text{power}$ fit).

9

4.8 The effects of cavity photons on qubit decoherence times

The T_2 vs power data from figure 15 may be combined with the $\bar{n}$ vs power data from figure 10 obtained in section 4.4 to obtain the relationship between T_2 and the average number of photons in the cavity. This is a useful result as it allows one to check if the expected number of photons in the cavity will lead to acceptable coherence times, an essential property of the qubit system. The result of combining the fits of figure 10 and 15 are shown in figure 16.
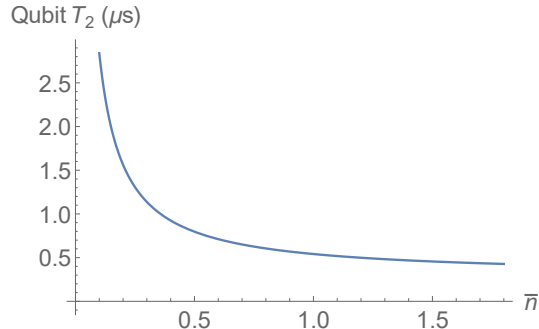

Figure 16: The expected relationship between T_2 coherence times of the qubit and the average photon number in the cavity, from combining the fits of figures 10 and 15. Restricted to the $\bar{n}, T_2$ range that we actually probed in experiment.

It is important to note that this plot is only valid when the photon number is the dominant effect in reducing the T_2 time. We see that the T_2 time of the qubit decreases as one over the average number of photons in the cavity, in agreement with equation 31. The effect is dramatic, with the presence of 0.36 average photons being sufficient to reduce the T_2 time to the sub-microsecond regime. The photon occupancy in our device at base temperatures was shown in section 4.5 to be $< 3.1\%$, corresponding to a potential T_2 time of $\sim 8\mu s$ for this device.

5 Conclusion

We have observed and classified the quantum behaviour of a transmon qubit inside a 3D superconducting microwave cavity. We found that the theoretical models for a two state qubit map well onto the behaviour of the first two levels of the transmon and demonstrated shifts in the qubit and cavity consistent with the dispersive limit of the Jaynes Cummings Hamiltonian. Using the dispersive shifts of the qubit, we demonstrated the coherent state population of the cavity and showed that it agreed with the theoretical model.

We went on to place limits on the effective cavity temperature and found for extremely low power (10^{-10}W) experiments $T_c < 144.5$mK corresponding to a single photon occupancy of less than 3.1%. This results in a potential T_2 time of $\sim 8\mu s$ for the device studied. Similarly we investigated the effective qubit temperature and found $T_q = 138.5 \pm 20$mK corresponding to a probability of being in state $|1\rangle$ of $10\pm4\%$. We investigated the T_2 coherence times of the transmon qubit when the cavity was driven at order nW, modelling accidental driving in experiments, and found them be on the order of μs. We classified the dependence of the T_2 time of the qubit on the average number of coherent photons in the cavity and found that the effects were dramatic. We observed the T_2 time of the qubit scaling as $1/\bar{n}$ as theoretically predicted, with an average photon occupancy of 0.36 being sufficient to reduce the T_2 time to the sub microsecond regime.

The results of this study show that if acceptable T_2 coherence times are to be achieved, it is imperative that the number of photons in the readout cavity must be kept to a minimum. The source of these photons in this study is artificial, intending to model accidental excitation of the cavity during other experiments. An interesting extension to this work would be to investigate photon numbers induced as a result of carrying out qubit operations, and to see how far readout powers can be pushed before they create too many photons. Investigation into the thermalisation of different stages of the fridge would also be interesting as despite the base temperature of 5mK, the effective temperatures of the qubit and cavity are still as much as 140mK. It would also be interesting to investigate these effects in multi-qubit systems, where qubit-qubit correlations may come into effect and readout methods become more complicated.

References

[1] T. D. Ladd, F. Jelezko, R. Laflamme, Y. Nakamura, C. Monroe, and J. L. O'Brien *Quantum Computers* Nature 464, 45 (2010).

[2] Devoret, M. H. and Schoelkopf, R. J. *Superconducting circuits for quantum information: An outlook.* Science 339, 1169–1174 (2013).

[3] A. Shnirman, G. Schön, and Z. Herman. *Quantum Manipulations of Small Josephson Junctions.* Phys. Rev. Lett. 79, 2371 (1997).

[4] C. Rigetti et al. *Superconducting qubit in waveguide cavity with coherence time approaching 0.1 ms.* arXiv:1202.5533 (2012).

[5] Christopher C. Gerry and Peter L. Knight. *Introductory Quantum Optics.* Cambridge university press (2005).
Field quantization: pp. 10-12
Qubit-cavity interaction: pp. 90-92

[6] S. J. Chapman, Q. Du, and M. D. Gunzburger. *A Ginzburg-Landau-type model of superconducting/normal junctions including Josephson junctions.* Europ. J. Appl. Math (1995).

[7] Michael J. Peterer. *Experiments on Multi-Level Superconducting Qubits and Coaxial Circuit QED.* A thesis submitted for the degree of Doctor of Philosophy, University of Oxford (2016).

[8] G Batey, A J Matthews and M Patton (Oxford Instruments Omicron NanoScience). *A new ultra-low-temperature cryogen-free experimental platform.* IOP Publishing (2014)

[9] Schuster, D. I. et al. *Resolving photon number states in a superconducting circuit.* Nature 445, 515–518 (2007).

[10] Blais, A., Huang, R., Wallraff, A., Girvin, S. and Schoelkopf, R. J. *Cavity quantum electrodynamics for superconducting electrical circuits: an architecture for quantum computation.* Phys. Rev. A 69, 062320 (2004).

[11] J. Koch et al. *Charge-insensitive qubit design derived from the Cooper pair box.* Phys. Rev. A 76, 04319 (2007).

[12] Gambetta, J. et al. *Qubit-photon interactions in a cavity: Measurement induced dephasing and number splitting.* Phys. Rev. A 74, 042318 (2006).

[13] Andrew W. Cross, David P. DiVincenzo, Barbara M. Terhal. *The Physical Implementation of Quantum Computation.* arXiv:0711.1556.

Acknowledgements

A Appendix

A.1 The coherent cavity states

We derive various results concerning the coherent exitation states $|\alpha\rangle$ of a cavity that satisfy $\hat{a}|\alpha\rangle = \alpha|\alpha\rangle$. Expanding in the basis $\{|n\rangle\}$ we can write

$$|\alpha\rangle = \sum_{n=0}^{\infty} C_n |n\rangle. \tag{35}$$

Then using $\hat{a}|n\rangle = \sqrt{n}|n-1\rangle$

$$\hat{a}|\alpha\rangle = \sum_{n=1}^{\infty} C_n \sqrt{n}|n-1\rangle \overset{!}{=} \alpha \sum_{n=0}^{\infty} C_n |n\rangle \tag{36}$$

The orthogonality of the states $|n\rangle$ then implies that the coefficients of $|n\rangle$ are the same on both sides:

$$C_n = \frac{\alpha}{\sqrt{n}} C_{n-1} \implies C_n = \frac{\alpha^n}{\sqrt{n!}} C_0 \tag{37}$$

Requiring normalization $\langle\alpha|\alpha\rangle = 1$ sets the constant C_0 and we obtain

$$|\alpha\rangle = e^{-\frac{1}{2}|\alpha|^2} \sum_{n=0}^{\infty} \frac{\alpha^n}{\sqrt{n!}} |n\rangle. \tag{38}$$

We also wish to find the value of $\langle\alpha|\hat{E}_x|\alpha\rangle$ where $\hat{E}_x$ is the electric field in a cavity with coherent states $|\alpha\rangle$. Substituting the expressions from equations 38 and 9 and defining $S \equiv (\hbar\omega_c/\epsilon_0 V)^{\frac{1}{2}} sin(kz)$ we have:

$$\langle\alpha|\hat{E}_x|\alpha\rangle = Se^{-|\alpha|^2} \sum_{n=0}^{\infty}\sum_{m=0}^{\infty} \frac{\alpha^n}{\sqrt{n!}}\frac{(\alpha^m)^*}{\sqrt{m!}} \langle m|\hat{a}+\hat{a}^\dagger|n\rangle$$

$$= Se^{-|\alpha|^2} \sum_{n=0}^{\infty}\sum_{m=0}^{\infty} \frac{\alpha^n}{\sqrt{n!}}\frac{(\alpha^m)^*}{\sqrt{m!}} (\delta_{m,n-1}\sqrt{n} + \delta_{m-1,n}\sqrt{m})$$

$$= Se^{-|\alpha|^2} \left[\sum_{m=0}^{\infty} \frac{\alpha^{m+1}}{\sqrt{(m+1)!}}\frac{(\alpha^m)^*}{\sqrt{m!}}\sqrt{m+1} \right.$$
$$\left. + \sum_{n=0}^{\infty} \frac{\alpha^n}{\sqrt{n!}}\frac{(\alpha^{n+1})^*}{\sqrt{(n+1)!}}\sqrt{n+1} \right]$$
$$\tag{39}$$

We note that the two terms in the square brackets are complex conjugates of one another and write

$$\langle\alpha|\,\hat{E}_x\,|\alpha\rangle = 2Se^{-|\alpha|^2}Re\left[\sum_{m=0}^{\infty}\frac{\alpha^{m+1}}{\sqrt{(m+1)!}}\frac{(\alpha^m)^*}{\sqrt{m!}}\sqrt{m+1}\right]$$

$$= 2Se^{-|\alpha|^2}Re\left[\alpha\sum_{m=0}^{\infty}\frac{|\alpha^m|^2}{m!}\right]$$

$$= 2SRe[\alpha]$$

$$= 2Re[\alpha]\left(\frac{\hbar\omega_c}{\epsilon_0 V}\right)^{\frac{1}{2}}sin(kz)$$

$$(40)$$

We see that if we make the associaiton

$$Re[\alpha] = \frac{1}{2}\left(\frac{2\omega_c}{\hbar}\right)^{\frac{1}{2}}2q(t) \qquad (41)$$

We recover the expression in equation 2 for the classical electric field (it may be useful to note that our harmonic oscillator has unit mass, so dimensionally factors of mass may have crept in, or crept out). It is also interesting to note that:

$$\langle\alpha|\,\hat{n}\,|\alpha\rangle = e^{-|\alpha|^2}\sum_{n=0}^{\infty}\sum_{m=0}^{\infty}\frac{\alpha^n}{\sqrt{n!}}\frac{(\alpha^m)^*}{\sqrt{m!}}\langle m|\,\hat{a}^\dagger\hat{a}\,|n\rangle$$

$$= e^{-|\alpha|^2}\sum_{n=0}^{\infty}\sum_{m=0}^{\infty}\frac{\alpha^n}{\sqrt{n!}}\frac{(\alpha^m)^*}{\sqrt{m!}}n\delta_{nm}$$

$$= e^{-|\alpha|^2}\sum_{n=0}^{\infty}\frac{|\alpha^n|^2}{n!}n$$

$$= e^{-|\alpha|^2}\sum_{n=1}^{\infty}|\alpha|^2\frac{|\alpha^{n-1}|^2}{(n-1)!}$$

$$= |\alpha|^2$$

$$(42)$$

A.2 Transmon mechanics

The energy level structure of the Transmon is derived, starting from a classical model of the cooper pair box (with reference to figure 2).

The classical dynamics of the Cooper pair box may be derived using an appropriate Lagrangian. Defining the node flux $\phi_j(t) = \int_{-\infty}^{t}V_j(t')dt'$, where V_j is the voltage across the junction, our Lagrangian will have a kinetic term given by the charging energies:

$$T = \frac{C_g}{2}\dot{\phi}_j^2 + \frac{C_j}{2}\dot{\phi}_j^2 \equiv \frac{C_\Sigma}{2}\dot{\phi}_j^2 \qquad (43)$$

The potential term will include the energy of the source V_g and a Josephson energy term $-E_j cos\left(2\pi\frac{\phi_j}{\phi_0}\right)$ [6], where ϕ_0 is the flux quantum $h/2e$. The source energy is V_gQ_g

where Q_g is the charge on the source side of the gate capacitor. This charge can be written as the voltage across the capacitor $(-\dot{\phi}_j)$ times the capacitance C_g. Putting this together the potential is:

$$U = -E_j cos\left(2\pi\frac{\phi_j}{\phi_0}\right) - v_g C_g\dot{\phi}_j \qquad (44)$$

So our classical Lagrangian is:

$$L = T - U = \frac{C_\Sigma}{2}\dot{\phi}_j^2 + E_j cos\left(2\pi\frac{\phi_j}{\phi_0}\right) + V_g C_g\dot{\phi}_j \quad (45)$$

The conjugate momentum is the charge on the island plus an effective offset charge created by the source:

$$Q_j = \frac{\partial L}{\partial\dot{\phi}_j} = C_\Sigma\dot{\phi}_j + V_g C_g. \qquad (46)$$

The classical Hamiltonian is then:

$$H = Q_j\dot{\phi}_j - L = E_c(n - n_g)^2 - E_j cos(\delta) \qquad (47)$$

Where we have defined the gate charge $n_g = C_gV_g/2e$, the charging energy $E_c = (2e)^2/2C_\Sigma$ and the superconducting phase difference $\delta = 2\pi\frac{\phi_j}{\phi_0}$. In this expression, n corresponds to the number of cooper pairs present in the superconducting island. By adding an additional capacitance C_S in parallel with the Josephson junction (see figure 2.b) we effectively have $C_\Delta \to C_\Delta + C_s$, increasing the ratio E_j/E_c. The limit $E_j/E_c \gg 1$ is the transmon regime.

To quantize this system we must enforce the canonical commutation relation $[\hat{\phi}, \hat{Q}] = i\hbar$. In our case it is more convenient to use the equivalent commutation relation $[\hat{\delta}, \hat{n}] = i$. We work in the charge basis $\{|n\rangle\}$ where $\hat{n}\,|n\rangle = n\,|n\rangle$. The charge operator $\hat{n}$ and the superconducting phase difference operator $\hat{\delta}$ are the fundamental objects of importance, obeying the canonical commuatation relation $[\hat{\delta}, \hat{n}] = i$. We show that $[\hat{n}, e^{\pm i\hat{\delta}}] = \pm e^{\pm i\hat{\delta}}$ and therefore that the operators $e^{\pm i\hat{\delta}}$ are the raising and lowering operators of the charge states $\{|n\rangle\}$ such that $e^{\pm i\hat{\delta}}\,|n\rangle = |n\pm 1\rangle$. Using the identity $[\hat{A}, \hat{B}\hat{C}] = \hat{B}[\hat{A}, \hat{C}] + [\hat{A}, \hat{B}]\hat{C}$ it is easily shown that

$$[\hat{A}, \hat{B}^n] = \sum_{m=0}^{n-1}\hat{B}^m[\hat{A}, \hat{B}]\hat{B}^{n-1-m}. \qquad (48)$$

From which it follows

$$[\hat{n}, (\pm i\hat{\delta})^n] = \sum_{m=0}^{n-1}(\pm i\hat{\delta})^m[\hat{n}, \pm i\hat{\delta}](\pm i\hat{\delta})^{n-1-m}$$

$$= \pm\sum_{m=0}^{n-1}(\pm i\hat{\delta})^{n-1} = \pm n(\pm i\hat{\delta})^{n-1}.$$

$$(49)$$

Then we have

$$[\hat{n}, e^{\pm i\hat{\delta}}] = \sum_{m=0}^{\infty}[\hat{n}, (\pm i\hat{\delta})^m]\frac{1}{m!}$$

$$= \sum_{m=0}^{\infty} \pm m(\pm i\hat{\delta})^{m-1}\frac{1}{m!} \qquad (50)$$

$$= \pm\sum_{m=1}^{\infty}(\pm i\hat{\delta})^{m-1}\frac{1}{(m-1)!} = \pm e^{\pm i\hat{\delta}}.$$

Using this we have

$$[\hat{n}, e^{\pm i\hat{\delta}}]\,|n\rangle = (\hat{n}e^{\pm i\hat{\delta}} - e^{\pm i\hat{\delta}}\hat{n})\,|n\rangle = \pm e^{\pm i\hat{\delta}}\,|n\rangle \implies$$

$$ne^{\pm i\hat{\delta}}\,|n\rangle = (n\pm 1)e^{\pm i\hat{\delta}}\,|n\rangle$$

$$\therefore e^{\pm i\hat{\delta}}\,|n\rangle = |n\pm 1\rangle.$$

$$(51)$$

So we see that the operators $e^{\pm i\hat{\delta}}$ are the raising and lowering operators for charge states. Using the fact that $cos(\hat{\delta}) = \frac{1}{2}(e^{i\hat{\delta}} + e^{-i\hat{\delta}})$ we obtain our quantized Hamiltonian:

$$H = \sum_n E_c(\hat{n} - n_g)\,|n\rangle\langle n| - \frac{E_j}{2}(|n\rangle\langle n+1| + |n+1\rangle\langle n|)$$

$$(52)$$

In the charge basis this Hamiltonian can be written as:

$$H = \begin{pmatrix} \ddots & & & & \\ & E_c(-1-n_g)^2 & -\frac{E_j}{2} & & \\ & -\frac{E_j}{2} & E_c(0-n_g)^2 & -\frac{E_j}{2} & \\ & & -\frac{E_j}{2} & E_c(1-n_g)^2 & \\ & & & & \ddots \end{pmatrix}$$

$$(53)$$

This can be easily diagonalized numerically to obtain the energy levels shown in figure 3.

A.3 Signal Processing

A.3.1 Signal generation

Controlling our signals to the required level of precision in the GHz regime directly is difficult so instead we control the *in-phase* (I) and *quaderature* (Q) components of our signal in a method known as *IQ-mixing*. This works by noting that for an arbitrary sinusoidal signal S we have

$$S = Acos(\omega t + \phi)$$
$$= Acos(\phi)cos(\omega t) - Asin(\phi)sin(\omega t)$$
$$= Icos(\omega t) - Qsin(\omega t) \qquad (54)$$
$$= Icos(\omega t) + Qcos(\omega t + \frac{\pi}{2}).$$

This enables us to accurately control the signals that we send into the fridge by using an *IQ mixer* as shown in figure 17. We see that the signals S_I and S_Q are multiplied

by $S_{IN}(\omega t)$ and $S_{IN}(\omega t + \pi/2)$ respectively to reproduce the desired signal in the same way as equation 54.
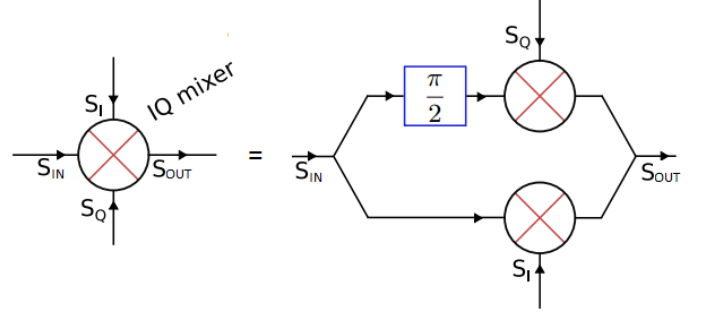

Figure 17: An IQ mixer [7]

In order to properly measure and control the system we have two such mixers, one for the readout signal and one for the qubit control pulses. The qubit control IQ is generated by an arbitrary waveform generator and the readout IQ is generated by an FPGA with a DAC as shown in figure 18.
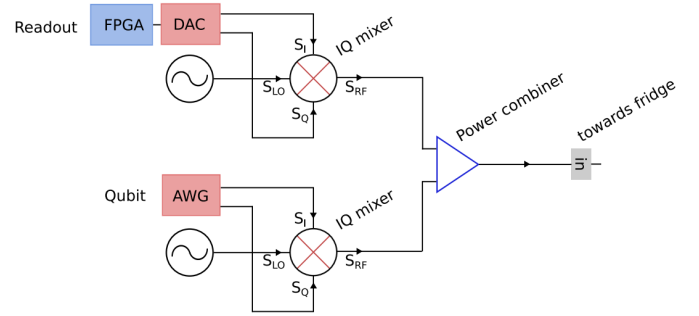

Figure 18: The signal generation setup [7]

A.3.2 Signal measurement

The transmitted signal that leaves the cavity is very small and is dominated by noise as it propagates out of the fridge. As a result, to obtain a reasonable signal to noise ratio many repetitions of the experiment must be averaged (we do this on the FPGA). The readout signal that we send in is in the GHz regime, which is too high to be digitized. As a result the signal must be mixed down to a lower frequency. This is achieved by mixing the incoming readout signal (at a frequency ω_R) with another signal at a frequency ω_o using an IQ mixer 'in reverse'. The resulting I and Q signals will then have two components at $\omega_R + \omega_o$ and $\omega_R - \omega_o$. The signal at $\omega_R + \omega_o$ is filtered out by a low pass filter and the result is down-converted quadratures at a frequency $\omega_d = \omega_R - \omega_o$, which can then be digitized. This down-conversion is shown in figure 19. This method is known as *heterodyne detection*.
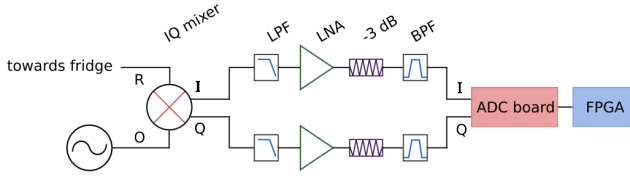
13

Figure 19: The signal down-conversion setup [7]

A.4 Lorentzian broadening

We show that the lineshape of a quantum state is broadened into a Lorentzian as a result of a characteristic decay time τ. Suppose the frequency of our state is ω_0, then we have $\psi \sim e^{i\omega_0 t}$. Introducing a characteristic decay time τ such that $|\psi|^2 \sim e^{-t/\tau}$, we can write $\psi \sim e^{i\omega_0 t - t/2\tau}$. Taking the fourier transform we obtain:

$$\psi(\omega) = \int_0^\infty \psi(t)e^{-i\omega t}dt \sim \int_0^\infty e^{i(\omega_0-\omega)t-t/2\tau}dt$$

$$= \frac{1}{\frac{1}{2\tau} - i(\omega_0 - \omega)} \implies |\psi(\omega)|^2 \sim \frac{1}{\frac{1}{4\tau^2} + (\omega_0 - \omega)^2} \quad (55)$$

This is the characteristic Lorentzian lineshape. To normalize it we write

$$|\psi(\omega)|^2 = \frac{A}{\frac{1}{4\tau^2} + (\omega - \omega_0)^2} \quad (56)$$

where A is some normalization constant to be found. We then require:

$$\int_0^\infty d\omega \frac{A}{\frac{1}{4\tau^2} + (\omega - \omega_0)^2} \overset{!}{=} 1 \quad (57)$$

Making the variable substitution $z = \omega - \omega_0$ we have

$$\frac{1}{A} \overset{!}{=} \int_{-\omega_0}^\infty dz \frac{1}{\frac{1}{4\tau^2} + z^2} \approx \int_{-\infty}^\infty dz \frac{1}{\frac{1}{4\tau^2} + z^2}$$

$$= \int_{-\infty}^\infty dz \frac{1}{\left(z - \frac{i}{2\tau}\right)\left(z + \frac{i}{2\tau}\right)} \quad (58)$$

$$= \lim_{R\to\infty} \oint_\Gamma dz \frac{1}{\left(z - \frac{i}{2\tau}\right)\left(z + \frac{i}{2\tau}\right)}$$

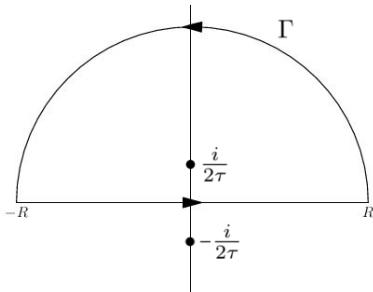Where Γ is the contour in the complex plane:

Figure 20: The contour Γ in the complex plane, with poles of the integrand labeled

This integral becomes just the integral along the real line as the contribution from the curved section $\to 0$ as $R \to \infty$. It can be easily evaluated using the Cauchy residue theorem

$$\oint_\Gamma f(z)dz = 2\pi i \sum_k R_{f,p_k}. \quad (59)$$

Here the sum runs over the poles p_k of f contained within the contour Γ and R_{f,p_k} is the residue of f at the pole p_k. The only relevant pole is at $\frac{+i}{2\tau}$ with residue $-i\tau$. Applying this we have:

$$\frac{1}{A} \approx \lim_{R\to\infty} \oint_\Gamma dz \frac{1}{\left(z - \frac{i}{2\tau}\right)\left(z + \frac{i}{2\tau}\right)} = 2\pi\tau \implies A = \frac{1}{2\pi\tau} \quad (60)$$

As a result our normalized Lorentzian reads

$$|\psi(\omega)|^2 = \frac{(2\pi\tau)^{-1}}{\frac{1}{4\tau^2} + (\omega - \omega_0)^2}. \quad (61)$$